

Development of a multiplex stimulated Raman microscope for spectral imaging through multi-channel lock-in detection

Keisuke Seto, Yoshinao Okuda, Eiji Tokunaga, and Takayoshi Kobayashi

Citation: [Review of Scientific Instruments](#) **84**, 083705 (2013); doi: 10.1063/1.4818670

View online: <http://dx.doi.org/10.1063/1.4818670>

View Table of Contents: <http://scitation.aip.org/content/aip/journal/rsi/84/8?ver=pdfcov>

Published by the [AIP Publishing](#)

Articles you may be interested in

[Hyperspectral imaging with in-line interferometric femtosecond stimulated Raman scattering spectroscopy](#)
J. Chem. Phys. **140**, 084201 (2014); 10.1063/1.4865939


[Standoff explosives trace detection and imaging by selective stimulated Raman scattering](#)
Appl. Phys. Lett. **103**, 061119 (2013); 10.1063/1.4817248

[Simultaneous detection of Raman scattering and near-infrared photoluminescence in one imaging microscope](#)
Rev. Sci. Instrum. **83**, 063709 (2012); 10.1063/1.4731684

[Light amplification by stimulated Raman scattering in AlGaAs-based photonic-crystal line-defect waveguides](#)
Appl. Phys. Lett. **93**, 051114 (2008); 10.1063/1.2965110

[A shear force feedback control system for near-field scanning optical microscopes without lock-in detection](#)
Rev. Sci. Instrum. **68**, 3093 (1997); 10.1063/1.1148247

JANIS Does your research require low temperatures? Contact Janis today.
Our engineers will assist you in choosing the best system for your application.



10 mK to 800 K
Cryocoolers
Dilution Refrigerator Systems
Micro-manipulated Probe Stations

LHe/LN₂ Cryostats
Magnet Systems

sales@janis.com www.janis.com
Click to view our product web page.

Development of a multiplex stimulated Raman microscope for spectral imaging through multi-channel lock-in detection

Keisuke Seto,^{1,2} Yoshinao Okuda,³ Eiji Tokunaga,³ and Takayoshi Kobayashi^{1,2,4,5}

¹*Department of Applied Physics and Chemistry and Institute for Laser Science, University of Electro-Communications, 1-5-1 Chofugaoka, Chofu, Tokyo 182-8585, Japan*

²*CREST, Japan Science and Technology Agency, 4-1-8 Honcho, Kawaguchi, Saitama 332-0012, Japan*

³*Department of Physics, Faculty of Science, Tokyo University of Science, 1-3 Kagurazaka, Shinjuku-ku, Tokyo 162-8601, Japan*

⁴*Department of Electrophysics, National Chiao-Tung University, Hsinchu 300, Taiwan*

⁵*Institute of Laser Engineering, Osaka University, 2-6 Yamada-oka, Suita, Osaka 565-0971, Japan*

(Received 28 May 2013; accepted 26 July 2013; published online 20 August 2013)

We report the development of a multiplex stimulated Raman microscope for spectral imaging through multi-channel lock-in detection with a single light source. A white pump beam is prepared with a piece of photonic crystal fiber (PCF). The system does not require the synchronization of plural light sources or the scanning of their wavelengths, and thus a jitter-free pair of pump and Stokes beams is obtained, and a high degree of temporal synchronization is attained in the spectra. The multi-channel lock-in detection (extended to 128 channels) enables the observation of pseudo-continuous stimulated Raman spectra, demonstrating the strong ability of qualitative analysis to identify various types of C–H stretching modes such as the symmetric and asymmetric modes of the methylene/methyl and aromatic groups. Images of a mixed film of polystyrene and polymethylmethacrylate are presented to demonstrate the system's spectral imaging ability. The spatial distribution of these materials is successfully captured through one-time imaging, although the noise of the white light pump beam generated with the PCF limits the system's imaging speed. © 2013 AIP Publishing LLC. [<http://dx.doi.org/10.1063/1.4818670>]

I. INTRODUCTION

Various chemical imaging methods have been developed to study the spatial dependency of the characteristics and functionalities of materials such as living cells from the distribution of their chemical structures. Raman imaging,^{1–3} in which an image is constructed using molecular vibrations, has several advantages. It enables contactless, non-destructive, non-labeled, and minimally invasive analysis, and is favorable for biological samples because of its insusceptibility to water compared with infrared (IR) microscopy. Spatial resolution is in the sub-micrometer order when visible probe light is used in Raman microscopy, whereas that of IR microscopy is in the 10- μm order.

The signal intensity of spontaneous Raman scattering, however, is significantly low, which results in a long acquisition time for the image. Imaging by coherent anti-Stokes Raman scattering (CARS) has been used to overcome this problem.^{4–8} This method produces signal intensity about three orders of magnitude higher than the spontaneous Raman microscopy, and has even achieved video-rate imaging.^{6,8} The CARS spectra, however, are distorted by non-resonant backgrounds (NRB) that complicate the assignment of signals and cause image artifacts. Optical and mathematical methods have been devised to overcome this problem.^{4,5}

Recently, stimulated Raman microscopy has been extensively used in high-speed chemical imaging, circumventing the NRB problem.^{9–19} Stimulated Raman spectra conserve high fidelity to spontaneous Raman spectra as they are NRB-free and the signal intensity is proportional to the Raman scat-

tering cross-section, which ensures the facile assignment of observed signals. The signal intensities are also proportional to the chemical concentration, which enables straightforward quantitative analysis.¹⁶ In the experimental setup of the stimulated Raman observation, precisely synchronized pulse lasers of at least two wavelengths are spatially overlapped on the sample. The higher energy laser in Fig. 1 is labeled the pump beam, and its counterpart is labeled the Stokes beam. When the difference between the photon energies is set at the vibrational energy of the molecule, one photon of the pump beam is annihilated and one photon of the Stokes beam is generated. This annihilation and generation is known as Raman loss and gain, and the stimulated Raman signals are observed as either loss or gain processes.

Stimulated Raman spectra can be observed with white light and monochromatic beams using a spectrograph²⁰ (upper right panel of Fig. 1). This method is applied for the stimulated Raman microscopy for spectral imaging with a charge-coupled device (CCD).⁹ A stimulated Raman spectrum is obtained by the quotient between the white light spectra with or without the monochromatic beam. The dynamic range of the CCD, however, is not very wide (~ 60 – 70 dB) and it is prone to saturation, which limits the signal to noise ratio (SNR) even when the pump laser is at an elevated intensity. To achieve a wider dynamic range, the lock-in detection of the pump or Stokes beam is used with the intensity modulation of the counterpart beam.^{12,21–23} The lock-in detection is essentially advantageous for weak signals as in stimulated Raman microscopy to reduce the light-source noise over other method like just signal accumulation with the CCD. The CCD

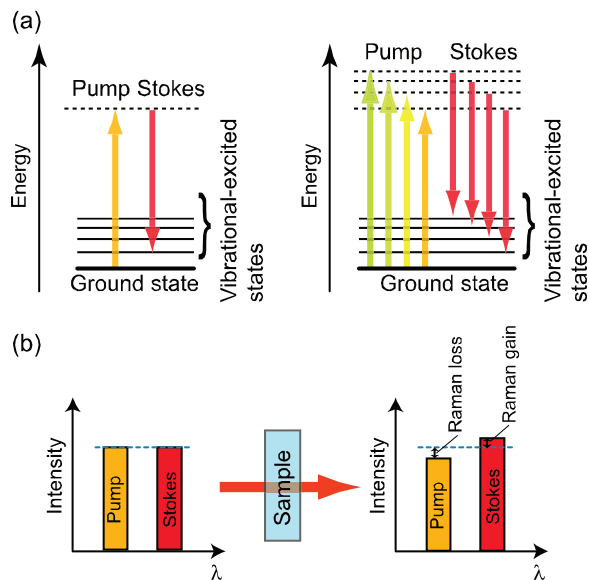


FIG. 1. Schematics of interaction between the pump beam and Stokes beam through a molecule with a vibrational energy level (a) and intensity modulation of the beams induced by Raman loss and gain (b). The left panel of (a) illustrates the detection of a single vibration of the molecule with the monochromatic pump and Stokes beams in conjunction with the molecular vibrational levels. The right panel of (a) illustrates our multiplex detection of the molecular vibrations with the broad-band pump beam and monochromatic Stokes beam.

accumulates all frequency components of the noise, whereas the lock-in detection rejects noise different from the lock-in frequency. Therefore, wider dynamic range and higher SNR are readily achieved with the lock-in detection. Single lock-in detection, however, is limited to a single detector. When the wavelengths of the two beams are fixed, only a single frequency Raman image is obtained on a single Raman band.

Several methods have been developed to obtain multi-color stimulated Raman images with the lock-in detection. One method involves scanning the difference in the wavelength, and is achieved by filtering the broad-band femtosecond pulse laser¹⁸ or controlling the temporal difference of the chirped femtosecond pulses (also known as spectral focusing).¹⁵ However, this method creates system complexities because it requires optical length maintenance during scanning or precise chirp control. Furthermore, the temporal synchronization among wavelengths is limited by the scan speed and the time-constant nature of the lock-in detection, which can cause spectral distortion and in turn render difficult the assignment of spectra and the quantitative analysis of chemical species. Another method involves the use of a few pump beams at various wavelengths that are modulated at different low frequencies and the lock-detection of the pump beams at a high modulation frequency of the Stokes beam, followed by Fourier transformation to distinguish the signals of the respective wavelengths.¹⁶ This method, however, limits the spectra to a few discrete wavelengths, thus limiting the spectral information, although the signals are observed with a high degree of temporal synchronization.

A single light source is desirable when preparing the pump and Stokes beams.¹⁵ Plural light sources may cause inter-source jitter, and precise synchronization^{12,24} is required

to achieve a high SNR, thus resulting in a highly complex and costly system.

We have developed a multiplex stimulated Raman microscope for spectral imaging that uses parallel lock-in detection at respective wavelengths with a 128-channel lock-in amplifier²⁵ and a white pump beam. Parallel lock-in detection is the most straightforward method of observing a spectral image using lock-in detection, and ensures a high degree of temporal synchronization among the respective Raman shifts. Furthermore, the light sources of the pump and Stokes beams come from a single mode-locked picosecond titanium-sapphire oscillator, which guarantees a jitter-free pump and Stokes beam pair. The white light pump beam is generated from a piece of photonic crystal fiber (PCF).^{4,15,26–28} The cross-sectional structure of the PCF reveals a core surrounded by regularly arranged air voids. These voids significantly reduce the effective refractive index of the core's surrounding area, which functions as the clad. The light in the PCF is tightly confined in the core owing to the large degree of difference in the refractive indices between the core and clad area. This tight confinement produces a large effective nonlinear coefficient that enables white light (supercontinuum) generation at just one order of kilo-watt peak power of the pulse laser from the oscillator.

II. SETUP

A. Optical setup

The experimental setup is shown in Fig. 2. The light source is a mode-locked titanium-sapphire oscillator (Mira 900P, COHERENT) pumped by a 532-nm diode-pumped solid-state laser (Verdi V5, COHERENT). The duration time, repetition rate, and average power are 2.5 ps, 76.3 MHz, and 450 mW, respectively. The back-reflected light from the optics is rejected by a Faraday isolator (I-7090C-2H, ISOWAVE) to protect the laser from instability induced by the interference of the reflected beam in the oscillator. The pulse laser beam is split into two by a beam splitter (BS1) with 60% transmissivity (T) and 40% reflectivity (R), corresponding to the pump line and Stokes line, respectively.

The 60% transmitted beam is introduced into a $2\times$ telescope to fill the entrance pupil of the microscope objective ($40\times$ magnification, numerical aperture (NA) = 0.65) and coupled with a 30-cm-long piece of PCF. The PCF (PM-NL-750, NKT) is of the polarization-maintaining type. Hence, the effective nonlinear coefficient is twice as large as that of the non-polarization-maintaining type when polarized light is coupled. The angle of the polarizing plane of the input light is adjusted by a half-wave plate to maximize the efficiency of the conversion into white light. The output light is collimated by another microscope objective lens ($40\times$, NA = 0.65). Components of more than 780 nm in the white light with unconverted 800 nm light are rejected by an inclined 800-nm cut-off interference dichroic mirror (FES0800, THOLABS).

The 40% reflected Stokes beam is chopped at a frequency of 1130 Hz with a mechanical chopper (Model 3501, New Focus). The beam is guided to an inverse telescope with a $f = 170$ -mm convex lens and $f = -150$ -mm concave lens.

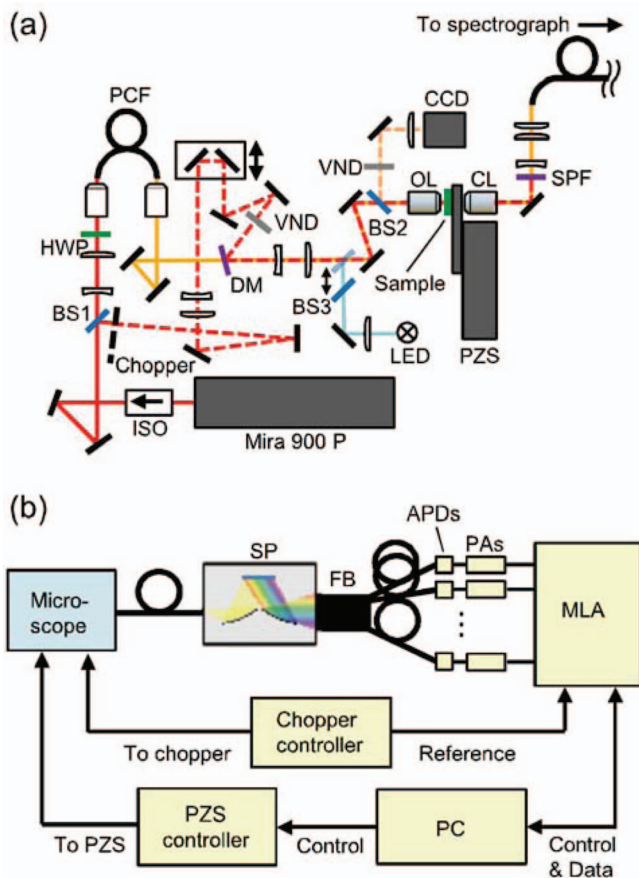


FIG. 2. Schematics of optical setup (a) and measurement system for spectral imaging by the multi-channel lock-in amplifier (b). (a) The red line indicates the Stokes beam at 800 nm, and the yellow line is the white pump beam. ISO: isolator that rejects backing scattered or reflected light; BS1: beam splitter for the Stokes and pump line; VND: variable neutral density filter to adjust power; HWP: half-wave plate that optimizes the polarizing plane; PCF: photonic crystal fiber; DM: dichroic mirror; OL: objective lens; CL: collector lens; PZS: piezo scanning stage; SPF: short-pass filter to reject the Stokes beam; BS2: beam splitter used to observe a sample and beam spots; BS3: beam splitter for epi-Köhler illumination; LED: light-emitting diode for epi-Köhler illumination; and CCD: charge-coupled device used to confirm the overlap of the beams and take photos of the samples. (b) SP: spectrograph; FB: fiber bundle; APDs: 128 avalanche photo diodes biased at 140 V; PAs: 128 10^7 gain transimpedance pre-amplifiers; MLA: 128-channel multi-channel lock-in amplifier; and PC: personal computer.

The functions of the inverse telescope are to adjust the beam diameter to fill the entrance pupil of the microscope objective to focus on the sample and to compensate for the axial chromatic aberration of the objective between the pump and Stokes beams. The collimated white pump beam and 800-nm Stokes beam are not focused at the same point because of the objective's chromatic aberration. Therefore, it is necessary to offset the focal point using the defocused inverse telescope, which allows the two beams to overlap at the same point. Compensation is performed by adjusting the inverse telescope's focus. The Stokes beam is sent to a delay stage to adjust the timing of its arrival in the sample to ensure that it overlaps temporally with the pump beam. The beam's power is adjusted with a variable neutral density filter (VND). The pump and Stokes beams are overlapped on the dichroic mirror (DM) and are aligned collinearly.

The beam diameters are expanded using a $1.5\times$ Galilean telescope with a $f = -100$ -mm concave lens and $f = 150$ -mm convex lens to fill the entrance pupil of the objective. When measuring a solution sample, a $10\times$, $NA = 0.25$ objective is used, whereas a $40\times$, $NA = 0.85$ objective is used in the measurement of solid plates or films. The beams are tightly focused on the sample by the objective, and the sample is placed on a computer-controlled piezo-scanning stage (MAX311D/M, THOLABS). The light reflected from the sample is collected with the objective and reflected by a pellicle beam splitter (BS2) with 92% T and 8% R to a CCD camera to confirm the spatial overlap of the beams. A sample image is also observed by the CCD camera using epi-Köhler illumination with a white light-emitting diode (LED). The beams transmitted through the sample are collimated by an objective ($20\times$, $NA = 0.4$). The collimated pump beam is sent to a $3\times$ Galilean telescope with a $f = -50$ -mm concave lens and $f = 150$ -mm convex lens through a 750-nm cut-off interference short-pass filter (FES0750, THOLABS) to reject the Stokes beam. The $3\times$ telescope optimizes the coupling efficiency to a subsequent optical fiber and reduces the beam's swing effect.

B. Multi-channel lock-in detection

The pump beam is coupled with a multi-mode optical fiber (core diameter: $600\ \mu\text{m}$; clad diameter: $660\ \mu\text{m}$; $NA = 0.22$) by a convex lens ($f = 100\ \text{mm}$) and sent to a 300-mm focal-length spectrograph (SpectraPro-300i, AC-TON) equipped with a 1200 g/mm grating. The specified resolution power is 0.1 nm, and the dispersion 2.7 nm/mm.

The spectrum is imaged onto the facet of a 16×128 quartz fiber bundle array in the spectrograph (Fig. 2(b)). The core and clad diameters are 100 and $110\ \mu\text{m}$, respectively, and the entrance size is $1.8\ \text{mm} \times 16.5\ \text{mm}$. The spectrum is divided into 128 wavelengths, and each of the 16 fibers of the same wavelength component is bundled. These 128 fibers are then coupled to 140-V biased avalanche photodiodes (APDs) (S5343, HAMAMATSU). The current signals from the APDs are converted to voltage signals by 10^7 gain transimpedance amplifiers (Model 7210/90, SIGNAL RECOVERY) and sent to four synchronized 32-channel digital signal-processing lock-in amplifiers (Model 7210, SIGNAL RECOVERY). The reference signal is generated by the chopper controller. Because the Raman loss signal is observed as the amplitude modulation depth (described later in the paper), it is preferable that the power of the white pump beam be kept as weak as possible to avoid sample degradation. Furthermore, the respective power levels of the channels are significantly weak, which requires the APDs and high gain preamplifiers.

III. EXPERIMENT

A. Wavelength calibration, wavelength range, spectrum of white light, and noise

The wavelengths are calibrated with the bright line spectra of a neon tube, and the sensitivities of the channels are

calibrated with a standard light source (color temperature = 2995 K \pm 5%) for a fluorescence spectrometer (F-4500, HITACHI). The center channels at the peak wavelengths of the bright lines are estimated by the peak position of the Gauss function fitted to these lines and measured with the 250- μ m entrance-slit width of the spectrograph. The calibration curve is prepared as a linear function of the channel, and the detection range is calculated by extrapolating this curve. The difference in wavenumber between neighboring channels (wavenumber step) is evaluated by dividing the detection range by the number of channels (128). The spectrum of the white pump beam generated by the PCF is measured with a spectrometer (USB2000+, Ocean Optics) through the DM. The noise spectrum of the white pump beam is observed with a photodiode (DET36A/M, THOLABS) and an oscilloscope (TDS2022B, TEKTRONIX). The spectrum is obtained through fast Fourier transformation of the signal.

The root mean square (RMS) electrical noise (EN) of the entire output is evaluated by the lock-in detected noises on the 128 channels at 1130 Hz of various time constants:

$$EN = \sqrt{\frac{1}{128} \sum_{i=1}^{128} \{e(i)\}^2}, \quad (1)$$

where $e(i)$ is the electrical noise observed on the i th channel. The electrical noise normalized to the white light signal (EN/I_P) is calculated as the RMS of the noise signals of the 128 channels divided by the lock-in detected signals of the chopped white light at a time constant of 10 s, with the 100- μ m slit width of the spectrograph:

$$\frac{EN}{I_P} = \sqrt{\frac{1}{128} \sum_{i=1}^{128} \left\{ \frac{e(i)}{I_P(i)} \right\}^2}, \quad (2)$$

where $I_P(i)$ is the signal of the chopped white light on the i th channel. The noise of the white pump beam (I_{PN}/I_P) is evaluated as the RMS of the lock-in detected signals of the 128 channels divided by the lock-in detected signals of the chopped white light at a time constant of 10 s:

$$\frac{I_{PN}}{I_P} = \sqrt{\frac{1}{128} \sum_{i=1}^{128} \left\{ \frac{I_{PN}(i)}{I_P(i)} \right\}^2}, \quad (3)$$

where $I_{PN}(i)$ is the noise signal of the white light observed on the i th channel.

B. Measurement of Raman loss spectra

To confirm the proposed system's ability to measure the Raman loss spectra, we measured cyclohexane, polystyrene (PS), and polymethylmethacrylate (PMMA). Cyclohexane was prepared in a 5-mm cell-length quartz cell, and PS and PMMA into 1.7-mm- and 1-mm-thick plates, respectively. The observed signals were normalized by the white light spectrum which was observed with the system to be corrected into Raman loss signals (modulation depths). The spontaneous Raman spectra of the substances were observed on NRS-3100 (JASCO) with 532-nm excitation and a resolution power of 1 cm^{-1} . The linearity of the Raman loss signals obtained by

our system was evaluated by the power dependence of the Stokes beam with cyclohexane in the quartz cell. The quantitative capability of the chemical concentration was evaluated by measuring cyclohexane and carbon tetrachloride mixtures at various molar ratios in the quartz cell.

C. Raman loss imaging

The piezo stage and lock-in amplifiers are computer-controlled (Lab View 8.5 software), and the spectra are observed point-by-point with the scanning of the sample. In this study, the samples were prepared as follows. A dispersion of 4- μ m PS beads (Invitrogen) was dropped onto a glass slide and left to dry. A mixed PS and PMMA film was prepared by drop-casting a 1:1 (by weight) mixed toluene solution of PS and PMMA on a glass slide.

IV. RESULTS AND DISCUSSION

A. Wavelength calibration, wavelength range, spectrum of white light, and noise

The bright line spectrum of the neon tube with the 250- μ m slit-width is shown in Fig. 3(a). The peak channels of the bright lines, which were estimated by fitting the Gauss function, are listed in Table I. The calibration curve was estimated as a linear function (Fig. 3(b)):

$$\lambda = 0.28666 \times \text{ch.} + 629.37 \text{ (nm)}, \quad (4)$$

where λ is the wavelength and ch. is the channel. The determination coefficient (R^2) is 0.99999, and the relationship between the wavelength and channel is sufficiently linear. The 1st and 128th channels are extrapolated to 629.65 and 666.06 nm, and these wavelengths correspond to 3382 and 2514 cm^{-1} Raman shifts, respectively. The detection range is 868 cm^{-1} , and the wavenumber step between neighboring channels is 6.78 cm^{-1} . The dispersion of the spectrograph is 2.7 nm/mm, and the resolution power with the 100- μ m entrance-slit width is 6.8 cm^{-1} at 630 nm. Thus, the Raman loss spectra shown hereafter were observed with the 100 μ m slit width. The spectrum of the white pump beam through the DM is shown in Fig. 4(a). The wavelength range is 780–575 nm, corresponding to 320–4890 cm^{-1} of the Raman shift range. The spectral range is sufficient to cover the frequency range of the molecular vibration.

TABLE I. Wavelengths of bright lines from the neon tube and estimated channels at the lines' peak.

λ^a (nm)	ch. ^b
630.47	3.7703
633.44	14.213
638.29	31.287
640.22	37.884
650.65	74.071
653.28	83.481
659.89	106.50

^a λ : Peak wavelength of the bright lines from the neon tube.

^bch.: Estimated channel at the peak of the bright line by fitting the Gauss function to the bright line observed with a 250- μ m entrance-slit width.

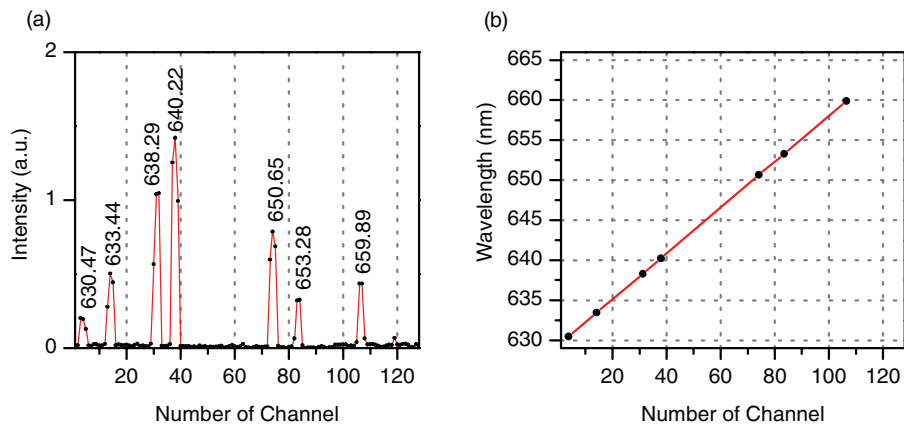


FIG. 3. The bright line spectrum from the neon tube with the 250- μm entrance-slit width on the spectrograph (a) and the correction curve (b). (a) The peak wavelengths of the neon bright lines are labeled on the corresponding bands, and (b) the dots represent the relationship between the peak channels estimated by fitting the Gauss function and the peak wavelengths. The red line is the calibration curve.

The system's electrical noise and the intensity noise of the white light are reported in Table II. The RMS electrical noise of the system is less than a few microvolts when the time constant is 1 s. The RMS electrical noise, normalized by the signal intensity of the white light with the 100- μm spectrograph slit width, is less than 10^{-5} when the time constant is 1 s. The electrical noise level is acceptable because the signal intensity of the white light is typically around 0.3 V at a spectrograph entrance-slit width of 100 μm , and the modulation depths of the Raman loss signals are typically 10^{-3} – 10^{-5} . The white light generated from the PCF, however, is significantly noisy, which requires a long time constant for lock-in detection, although the system is simple. The RMS intensity noise is around 2×10^{-4} for a time constant of 1 s, which limits the SNR of the Raman loss signal.

The noise spectra in kilo-hertz region and mega-hertz region are shown in Figs. 4(b)–4(d). The noise is white from the kilo-hertz to 10 mega-hertz. Although mega-hertz order high frequency lock-in detection is often used to reduce observed noise,^{10,12,13,16–19,29} in the present case, it cannot be

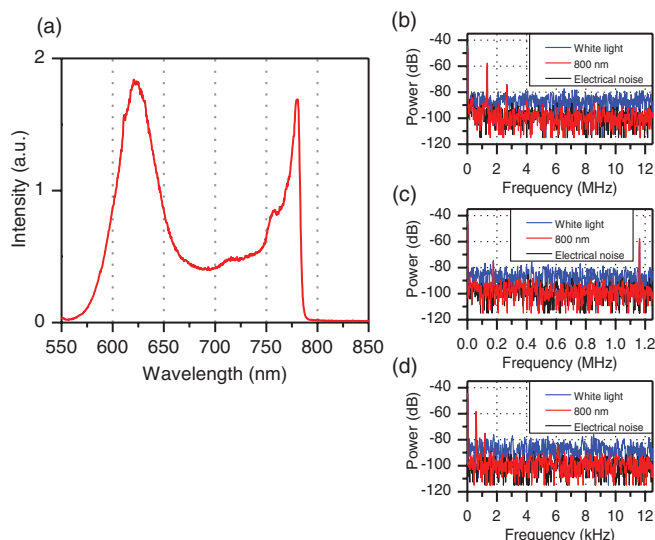


FIG. 4. Spectrum of the white pump beam through the dichroic mirror (a); light noise spectra in 0–12.5 MHz (b); in 0–1.25 MHz (c); and in 0–12.5 kHz (d).

reduced with mega-hertz lock-in detection. This frequency independent nature of the white light noise is also mentioned by another research group.³⁰

Thus, noise cancellation by some form of balanced detection^{31,32} is required for high-speed imaging. Because the noise varies widely by wavelength, and transmission through a sample varies during imaging, the application of balanced detection to our Raman-loss detection system requires the signal and reference beams to have exactly the same optical path from the microscope through the spectrograph to the APDs. Collinear balanced detection (CBD)³² is a balanced-detection method in which the two have the same optical path, but it requires megahertz-order high frequency lock-in detection for realistic optics, and its performance depends on the equal splitting of the pump beam. In our system, the equal splitting of the pump beam is required in a broad wavelength range, which is not realistic with practical optics. We plan to develop a new balanced-detection method in a future study.

B. Measurement of Raman loss spectra

Figs. 5(a) and 5(b) show the observed spectra of cyclohexane, PS, and PMMA on the proposed system and their

TABLE II. RMS electrical noise and RMS intensity noise of white pump beam.

TC^a (ms)	EN^b (μV)	EN/IP^c (10^{-4})	$I_P N/IP^d$ (10^{-4})
3	19	1.4	28
10	11	0.81	25
30	5.9	0.43	12
100	3.1	0.23	5.9
300	2.1	0.16	3.7
1000	1.4	0.099	2.1
3000	0.77	0.060	1.2
10 000	0.47	0.033	0.71

^a TC : Time constant of the lock-in detection.

^b EN : RMS electrical noise of the system output.

^c EN/IP : RMS electrical noise relative to the white pump beam signal at the 100 μm entrance-slit width on the spectrograph.

^d $I_P N/IP$: RMS intensity noise of the white pump beam.

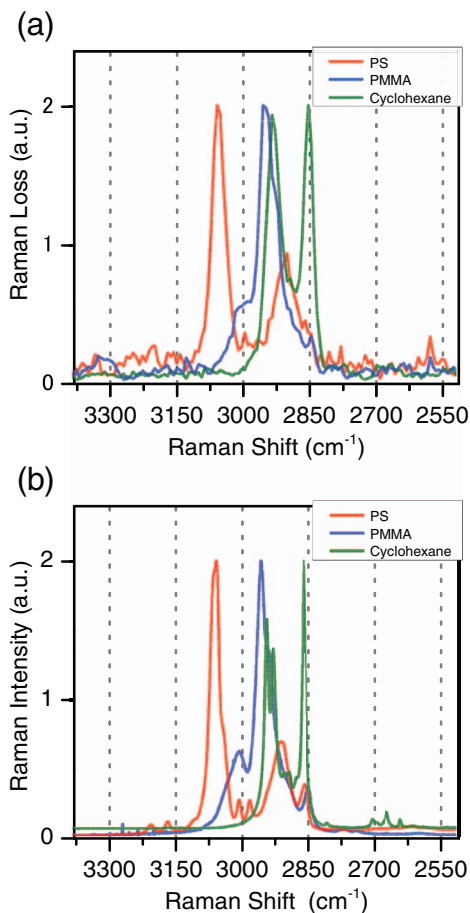


FIG. 5. Stimulated Raman loss spectra of polystyrene (PS), polymethylmethacrylate (PMMA), and cyclohexane observed with the system constructed in this study (a) and spontaneous Raman spectra of the same samples (b).

spontaneous Raman spectra, respectively. The average power of the white pump beam and 800-nm Stokes beam are 3.0 and 53.4 mW, respectively, and the time constant of the lock-in detection is 10 s. The spectra on our system conform to the spontaneous Raman spectra. They disappear when the white pump beam and/or 800-nm Stokes beam are blocked, or the focal spots overlap and/or the time delay is displaced. The Raman loss signal is proportional to the Raman scattering cross-section given in the following equation:²⁹

$$\frac{\Delta I_P}{I_P} \propto N \times \sigma_{Raman} \times I_S, \quad (5)$$

where I_P , ΔI_P , I_S , N , and σ_{Raman} are the pump intensity, reduction in pump intensity, Stokes intensity, concentration, and Raman scattering cross-section, respectively. The relation ensures the high fidelity of the stimulated Raman loss spectra to the spontaneous Raman spectra. Thus, the results confirm that the stimulated Raman loss spectra are observed on our system. They also demonstrate the strong capability of qualitative analysis to identify the C–H symmetric stretching ($\sim 2850 \text{ cm}^{-1}$) and asymmetric stretching ($\sim 2930 \text{ cm}^{-1}$) modes of the methylene groups (cyclohexane), CH_3 symmetric stretching ($\sim 2870 \text{ cm}^{-1}$), and asymmetric stretching ($\sim 2960 \text{ cm}^{-1}$) modes of the methyl groups (PMMA), and aromatic C–H stretching mode ($\sim 3030 \text{ cm}^{-1}$, PS).

Fig. 6(a) shows the Raman loss spectra of cyclohexane with various powers of the Stokes beam in the sample position. The average power of the white-light pump beam is 1.1 mW. The Raman loss intensity at the 65th channel, which is the strongest peak in the spectra and corresponds to a white-light spectrum wavelength of 648.00 nm and 2932 cm^{-1} Raman shift, is linearly dependent on the power (Fig. 6(b)). The determination coefficient (R^2) is 0.998. The Raman loss signal is linearly dependent on the Stokes power, as in Eq. (5), thus confirming the system's linearity. Fig. 6(c) shows the Raman loss spectra of cyclohexane diluted with carbon tetrachloride to various concentrations. The average power of the white pump beam and the power of the 800-nm Stokes beam are 1.1 and 83.3 mW, respectively. No signal is observed in the spectra of carbon tetrachloride (indicated as 0 mol/l) in the observed range of Raman shifts. The Raman loss intensity at the 65th channel exhibits excellent linear dependence on the concentration (Fig. 6(d)). The determination coefficient (R^2) of the linearity is 0.999. These results indicate the system's high degree of quantitative capability, as predicted by Eq. (5).

C. Raman loss imaging

Fig. 7 presents a CCD image of the $4\text{-}\mu\text{m}$ PS beads by white LED illumination and an image of the $4\text{-}\mu\text{m}$ PS beads in the same area based on the summation of the signals on the 40–50th channels ($3103\text{--}3033 \text{ cm}^{-1}$ Raman shifts). The image and pixel sizes are $10 \mu\text{m} \times 10 \mu\text{m}$ and $0.25 \mu\text{m} \times 0.25 \mu\text{m}$, respectively. The average power of the white pump beam and the power of the 800-nm Stokes beam are 0.42 and 67.6 mW, respectively, and the time constant and dwelling times are 300 ms and 600 ms, respectively. The spatial distribution of the lock-in signal strengths conforms to the PS beads observed by the CCD. The averaged spectrum at the centers of the PS beads (Fig. 7(c)) conforms to the spontaneous Raman spectrum of PS (Fig. 5(b)), which confirms that the image strength is proportional to the Raman loss signal intensity of PS. Thus, the $4\text{-}\mu\text{m}$ PS beads are successfully imaged.

The CCD image of the mixed PS and PMMA film and the Raman loss images of the same area are shown in Figs. 8(a)–8(c). The black lines in the CCD image are cracks. The image and pixel sizes are $20 \mu\text{m} \times 20 \mu\text{m}$ and $0.5 \mu\text{m} \times 0.5 \mu\text{m}$, respectively. The average power of the white pump beam and the power of the 800 nm Stokes beam are 3.6 and 54.5 mW, respectively, and the time constant and dwelling times are 1000 ms and 2000 ms, respectively. These images are obtained through single imaging, and image (b) is constructed on the summation of the signals from the 40–50th channels ($3103\text{--}3033 \text{ cm}^{-1}$ Raman shift), whereas (c) is constructed on the signals from the 55th to 65th channels ($2998\text{--}2930 \text{ cm}^{-1}$). The averaged Raman loss spectrum of the area in which intense signals in the range of the 40–50th channels are observed (surrounded by a green square in Figs. 8(b) and 8(c)) is shown in Fig. 8(d), and that of the 55–65th channels (surrounded by a red square) is shown in Fig. 8(e). The PS Raman bands are dominant in Fig. 8(d), and the PMMA band (which appears around 2960 cm^{-1}) is more intense in the counterpart

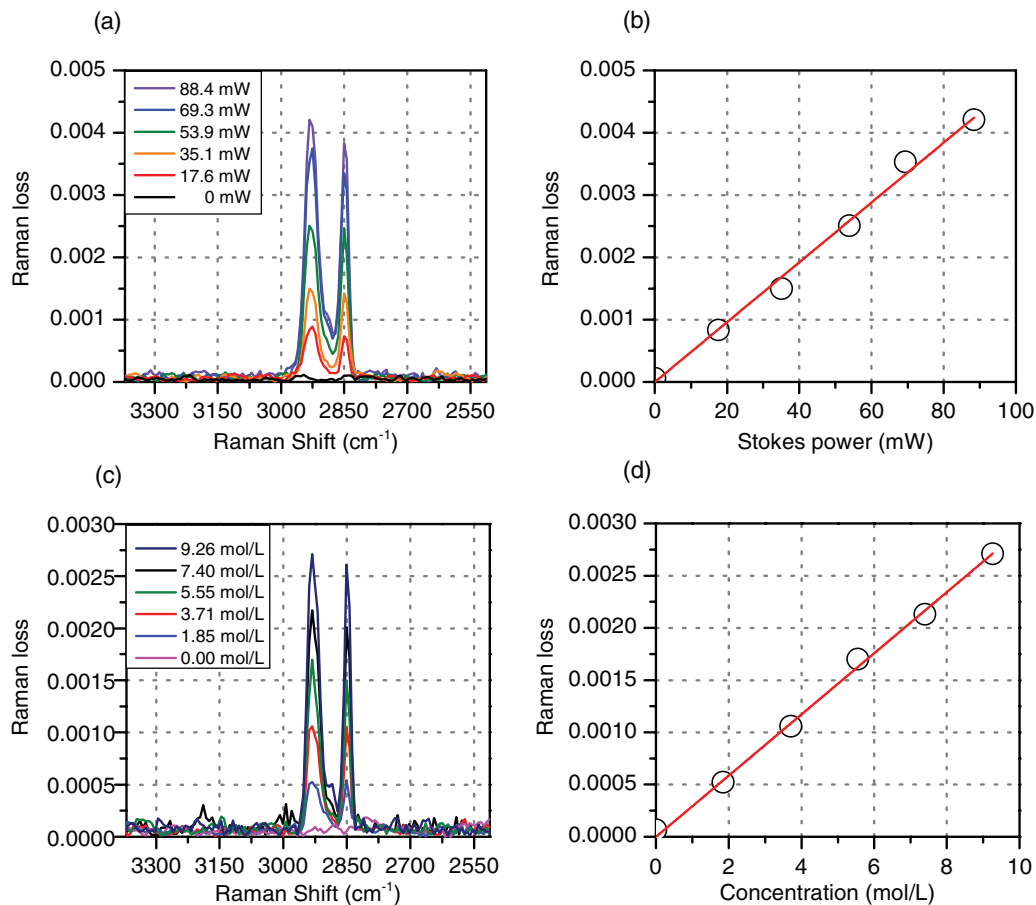


FIG. 6. The Raman loss spectra of cyclohexane at various Stokes beam powers (a); the relationship between the Raman loss signal at the 65th channel (the strongest peak of cyclohexane) and the power (b); the Raman loss spectra of cyclohexane diluted by carbon tetrachloride at various concentrations (c); and the relationship between the Raman loss signal at the 65th channel and the concentration.

(Fig. 8(e)). Although the polymers appear to be mixed homogeneously using the CCD, the differences in contrast of the images in Figs. 8(b) and 8(c) suggest a different distribution and some aggregate material structures. The inhomogeneous distribution of mixed polymer films has also been observed by another research group.¹

Note that the multi-channel detection of the spectra ensures a high degree of temporal synchronization among the Raman bands, which minimizes the spectral distortion caused by sample degradation during measurement. Such distortion

can create difficulties in assigning the Raman bands and/or in quantitative analysis. Temporal synchronization is also important in the high-speed multi-color imaging of moving samples such as living cells and fluids.

The proposed method is highly suited for measurements which require high precision of Raman shifts such as imaging by Raman shifts and/or bandwidth variations since this method does not require wavenumber scanning and is robust in Raman shifts. This imaging is applicable to, for example, the detection of surface defect and spatial non-uniformity of

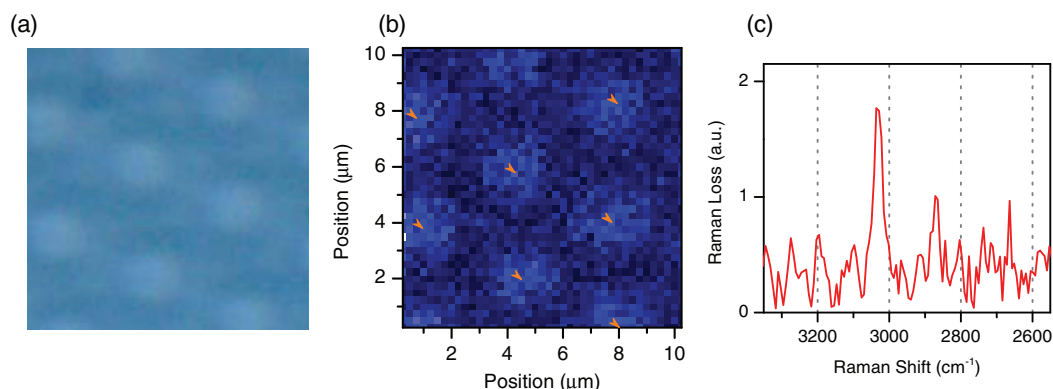


FIG. 7. CCD image of the 4- μm PS beads ($10 \times 10 \mu\text{m}$ area) (a); image of the same area constructed on the summation of the signals of the 40–50th channels (b); and the averaged spectrum of the spectra at the centers of the beads (indicated by the orange marks in (b)) (c).

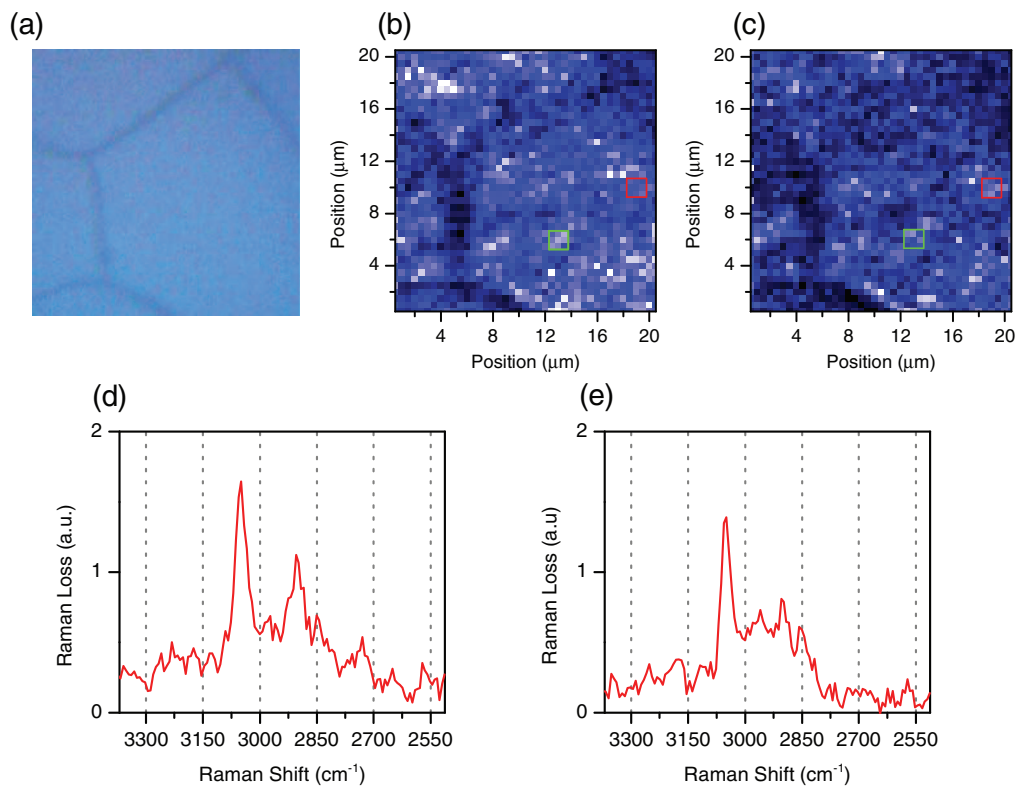


FIG. 8. CCD image of the mixed polymer film of PS and PMMA ($20\ \mu\text{m} \times 20\ \mu\text{m}$ area) (a); image of the same area based on the summation of the signals of the 40–50th channels ($3103\text{--}3033\ \text{cm}^{-1}$ Raman shift) (b); image based on the summation of the 55–65th channels ($2998\text{--}2930\ \text{cm}^{-1}$) (c); averaged spectrum in the area of the strong signals of the 40–50th channels (surrounded by the green square) (d); and the averaged spectrum in the area of the strong signals of the 55–65th channels (surrounded by the red square) (e).

ceramics, inorganics, and doped-polymer film systems used in automotive, plastic displays, and others which are important in industry.

The chromatic aberration of the microscope objective causes the displacement of the focus points between the pump and Stokes beams. This problem not only causes a significant reduction in the intensity of the Raman loss signals, but also creates an artifact signal via the thermal-lens effect.^{33,34} When the artifact generated by the thermal effect appears, the baseline of the spectrum shifts, and the contrast between the Raman signal and background is reduced. This aberration can be corrected by offsetting the focal point of the Stokes beam with the lens pair before the objective. However, the correction is possible only in a narrow wavelength detection range. Although the reflection objective can be used, the NA and throughput of this type of objective are limited. Thus, a more sophisticated achromatic objective correction with a high NA would be desirable. In our system, the Raman loss signals are easily distinguishable from this type of artifact, which is not the case with the conventional single wavelength detection method.

V. CONCLUSION

We have developed a multiplex stimulated Raman microscope for spectral imaging with multi-channel lock-in detection and a white pump beam with a single light source. Our system requires no synchronization of plural light sources

or wavelength scanning. In addition, it suffers no jitter or optical-length mismatch problems arising from the multiple sources with different wavelengths used in conventional stimulated Raman microscopy. The ADPs and high-gain preamplifiers eliminate the need for optical amplification of the white pump beam, thereby reducing the possibility of sample degradation and simplifying the system. The 128-channel lock-in detection of the white pump beam enables observation of pseudo-continuous Raman loss spectra and demonstrates strong qualitative capability in identifying various kinds of C–H stretching modes. The multi-channel lock-in detection improves imaging not only by increasing the speed being multiplied by the channel number, but also by alleviating problems such as laser fluctuations and sample damage by simultaneously measuring the full Raman spectral range of interest. The noise of the white light generated by the PCF limits high-speed imaging, but we expect to overcome this problem with a new balanced detection method in a future study.

ACKNOWLEDGMENTS

This study was financially supported by a joint research project at the Institute of Laser Engineering, Osaka University, under Contract No. B1-27.

¹M. D. Schaeberle, C. G. Karakatsanis, C. J. Lau, and P. J. Treado, *Anal. Chem.* **67**, 4316–4321 (1995).

²M. Okada, N. I. Smith, A. F. Palonpon, H. Endo, S. Kawata, M. Sodeoka, and K. Fujita, *Proc. Natl. Acad. Sci. U.S.A.* **109**, 28–32 (2012).

- ³K. Seto and Y. Furukawa, *J. Raman Spectrosc.* **43**, 2015–2019 (2012).
- ⁴M. Okuno, H. Kano, P. Leproux, V. Couderc, J. P. R. Day, M. Bonn, and H.-o. Hamaguchi, *Angew. Chem., Int. Ed.* **49**, 6773–6777 (2010).
- ⁵T. Suzuki and K. Misawa, *Opt. Express* **19**, 11463–11470 (2011).
- ⁶C. L. Evans, E. O. Potma, M. Puoris'haag, D. Côté, C. P. Lin, and X. S. Xie, *Proc. Natl. Acad. Sci. U.S.A.* **102**, 16807–16812 (2005).
- ⁷M. D. Duncan, J. Reintjes, and T. J. Manuccia, *Opt. Lett.* **7**, 350–352 (1982).
- ⁸T. Meyer, N. Bergner, A. Medyukhina, B. Dietzek, C. Krafft, B. F. M. Romeike, R. Reichart, R. Kalf, and J. Popp, *J. Biophoton.* **5**, 729–733 (2012).
- ⁹E. Ploetz, S. Laimgruber, S. Berner, W. Zinth, and P. Gilch, *Appl. Phys. B* **87**, 389–393 (2007).
- ¹⁰P. Nandakumar, A. Kovalev, and A. Volkmer, *New J. Phys.* **11**, 033026 (2009).
- ¹¹E. Ploetz, B. Marx, T. Klein, R. Huber, and P. Gilch, *Opt. Express* **17**, 18612–18620 (2009).
- ¹²Y. Ozeki, Y. Kitagawa, K. Sumimura, N. Nishizawa, W. Umemura, S. i. Kajiyama, K. Fukui, and K. Itoh, *Opt. Express* **18**, 13708–13719 (2010).
- ¹³B. G. Saar, C. W. Freudiger, J. Reichman, C. M. Stanley, G. R. Holtom, and X. S. Xie, *Science* **330**, 1368–1370 (2010).
- ¹⁴E. R. Andresen, P. Berto, and H. Rigneault, *Opt. Lett.* **36**, 2387–2389 (2011).
- ¹⁵H. T. Beier, G. D. Noojin, and B. A. Rockwell, *Opt. Express* **19**, 18885–18892 (2011).
- ¹⁶D. Fu, F.-K. Lu, X. Zhang, C. Freudiger, D. R. Pernik, G. Holtom, and X. S. Xie, *J. Am. Chem. Soc.* **134**, 3623–3626 (2012).
- ¹⁷C. W. Freudiger, W. Min, G. R. Holtom, B. Xu, M. Dantus, and X. S. Xie, *Nature Photon.* **5**, 103–109 (2011).
- ¹⁸Y. Ozeki, W. Umemura, K. Sumimura, N. Nishizawa, K. Fukui, and K. Itoh, *Opt. Lett.* **37**, 431–433 (2012).
- ¹⁹X. Zhang, M. B. J. Roeffaers, S. Basu, J. R. Daniele, D. Fu, C. W. Freudiger, G. R. Holtom, and X. S. Xie, *ChemPhysChem* **13**, 1054–1059 (2012).
- ²⁰W. J. Jones and B. P. Stoicheff, *Phys. Rev. Lett.* **13**, 657–659 (1964).
- ²¹Y. Ozeki, F. Dake, S. i. Kajiyama, K. Fukui, and K. Itoh, *Opt. Express* **17**, 3651–3658 (2009).
- ²²A. Owyong and E. D. Jones, *Opt. Lett.* **1**, 152–154 (1977).
- ²³A. Owyong, *Opt. Commun.* **22**, 323–328 (1977).
- ²⁴D. J. Jones, E. O. Potma, J.-X. Cheng, B. Burfeindt, Y. Pang, J. Ye, and X. S. Xie, *Rev. Sci. Instrum.* **73**, 2843–2848 (2002).
- ²⁵T. Kobayashi, W. Zhuan, and I. Izumi, *New J. Phys.* **10**, 065009 (2008).
- ²⁶A. V. Husakou and J. Herrmann, *Phys. Rev. Lett.* **87**, 203901 (2001).
- ²⁷J. Herrmann, U. Griebner, N. Zhavoronkov, A. Husakou, D. Nickel, J. C. Knight, W. J. Wadsworth, P. S. J. Russell, and G. Korn, *Phys. Rev. Lett.* **88**, 173901 (2002).
- ²⁸H. Kano and H.-O. Hamaguchi, *Opt. Lett.* **28**, 2360–2362 (2003).
- ²⁹C. W. Freudiger, W. Min, B. G. Saar, S. Lu, G. R. Holtom, C. He, J. C. Tsai, J. X. Kang, and X. S. Xie, *Science* **322**, 1857–1860 (2008).
- ³⁰K. L. Corwin, N. R. Newbury, J. M. Dudley, S. Coen, S. A. Diddams, K. Weber, and R. S. Windeler, *Phys. Rev. Lett.* **90**, 113904 (2003).
- ³¹A. Gambetta, V. Kumar, G. Grancini, D. Polli, R. Ramponi, G. Cerullo, and M. Marangoni, *Opt. Lett.* **35**, 226–228 (2010).
- ³²K. Nose, Y. Ozeki, T. Kishi, K. Sumimura, N. Nishizawa, K. Fukui, Y. Kanematsu, and K. Itoh, *Opt. Express* **20**, 13958–13965 (2012).
- ³³M. Tokeshi, M. Uchida, A. Hibara, T. Sawada, and T. Kitamori, *Anal. Chem.* **73**, 2112–2116 (2001).
- ³⁴E. Tamaki, K. Sato, M. Tokeshi, K. Sato, M. Aihara, and T. Kitamori, *Anal. Chem.* **74**, 1560–1564 (2002).